

Evidence for powerful winds and the associated reverse shock as the origin of the Fermi bubbles

Yutaka Fujita^{1*}

¹*Department of Physics, Graduate School of Science, Tokyo Metropolitan University,
1-1 Minami-Osawa, Hachioji-shi, Tokyo 192-0397, Japan*

Accepted XXX. Received YYY; in original form ZZZ

ABSTRACT

The Fermi bubbles are large gamma-ray-emitting structures. They are symmetric about the Galactic Centre (GC), and their creation is therefore attributed to intensive energy injection at the GC. In this study, we focus on the non-equilibrium X-ray gas structures associated with the bubbles. We show that a combination of the density, temperature, and shock age profiles of the X-ray gas can be used to distinguish the energy injection mechanisms. By comparing the results of numerical simulations with observations, we indicate that the bubbles were created by a fast wind from the GC because it generates a strong reverse shock and reproduces the observed temperature peak there. On the other hand, instantaneous energy injection at the GC cannot reproduce the temperature profile. The wind had a speed of $\sim 1000 \text{ km s}^{-1}$, and blew for $\sim 10^7 \text{ yr}$. Because the mass flux of the wind is large, the entrainment of interstellar gas by wide-angle outflows from the black hole is required. Thus, the wind may be the same as active galactic nuclei outflows often observed in other galaxies and thought to regulate the growth of galaxies and their central black holes.

Key words: ISM: jets and outflows – Galaxy: centre – Galaxy: halo

1 INTRODUCTION

The Fermi bubbles are large gamma-ray-emitting structures extending $\sim \pm 50^\circ$ above and below the Galactic plane (Dobler et al. 2010; Su et al. 2010; Ackermann et al. 2014), and related structures have been discovered based on X-ray (Keshet & Gurwicz 2018) and radio observations (Finkbeiner 2004; Dobler & Finkbeiner 2008; Planck Collaboration 2013). However, the origin of the Fermi bubbles, for example, the instantaneous explosive activity of a central supermassive black hole (Sagittarius A*^{*}; Guo & Mathews 2012; Fujita et al. 2013, 2014; Zhang & Guo 2020; Mondal et al. 2022; Yang et al. 2022), winds from the black hole (Zubovas & Nayakshin 2012; Mou et al. 2014, 2015), a starburst (Carretti et al. 2013; Lacki 2014; Sarkar et al. 2015), or steady star-formation activity (Crocker & Aharonian 2011; Crocker 2012, see also Narayanan & Slatyer 2017), has been debated.

Peculiar X-ray structures were recognised in the direction of the Galactic Centre (GC) even before the discovery of Fermi bubbles in gamma rays. In particular, the regions corresponding to high X-ray and radio wave intensities are called the North Polar Spur and Loop I (Snowden et al. 1995). There has been discussion on whether their origin is from a nearby supernova remnant or galactic-scale structures located near the GC (Salter 1983; Sofue 2000; Bland-Hawthorn & Cohen 2003). However, recent eROSITA telescope observations have shown that these X-ray structures are part of a larger structure encompassing the Fermi bubbles, which

means that their association with the galactic structure and Fermi bubbles has been confirmed (Predehl et al. 2020). Consequently, the properties of the X-ray structures are related to the formation process of the Fermi bubbles. Previous studies have mainly focused on the morphology of X-ray structures that reflect gas density distributions (e.g. Yang et al. 2022). By contrast, in this study, we demonstrate that the combined analysis of the density, temperature, and shock age profiles of the gases based on X-rays is a powerful tool for distinguishing the energy-injection mechanisms of the Fermi bubbles. Importantly, this helps us understand the origin of the Fermi bubbles. Here, the shock age is defined as the time elapsed since the passing of a shock wave through a gas element.

The paper is organised as follows. In Section 2, we explain our models and numerical setup. In section 3, we compare our simulation results with observations, and show that the Fermi bubbles should have been created by a fast wind. In section 4, we discuss the origin of the wind based on the parameters derived in Section 3. The conclusion of this paper is presented in Section 5.

2 MODELS

To study the dependence of the X-ray gas profiles on different energy-injection mechanisms at the GC, we performed one-dimensional (1D) Lagrangian hydrodynamic simulations of shock propagation from the GC (Bodenheimer et al. 2007), regarding the Fermi bubbles as a single bubble centred on the GC. The one-dimensionality of the code enables unknown pa-

* E-mail: y-fujita@tmu.ac.jp

parameters to be specified by performing $\sim 10^4$ simulations and comparing the results with observations. Because the actual Fermi bubbles are not spherically symmetric, we adopted the volume-averaged radius ($r \sim 4$ kpc) as the typical radius of the bubbles (Crocker et al. 2015). Radiative cooling is ignored because the densities of the ejecta and halo gas are low. The code allows us to explicitly determine the shock age by measuring the time elapsed since shock passage at each gas element. The position of the shock wave can be identified by searching for the position where the flow converges.

2.1 Galaxy model

The gravitational potential is given by

$$\Phi = \Phi_{\text{halo}} + \Phi_{\text{disk}} + \Phi_{\text{bulge}}, \quad (1)$$

where

$$\Phi_{\text{halo}}(r) = v_{\text{halo}}^2 \ln(r^2 + d_h^2) \quad (2)$$

is the halo potential,

$$\Phi_{\text{disk}}(r) = -\frac{GM_{\text{disk}}}{a + \sqrt{r^2 + b^2}} \quad (3)$$

is the potential known as the Miyamoto-Nagai disk, G is the gravitational constant (Miyamoto & Nagai 1975), and

$$\Phi_{\text{bulge}}(r) = -\frac{GM_{\text{bulge}}}{r + d_b} \quad (4)$$

is the potential, known as the Hernquist stellar bulge. The adopted values are $v_{\text{halo}} = 131.5 \text{ km s}^{-1}$, $d_h = 12$ kpc, $M_{\text{disk}} = 10^{11} M_{\odot}$, $a = 6.5$ kpc, $b = 0.26$ kpc, $M_{\text{bulge}} = 3.4 \times 10^{10} M_{\odot}$, and $d_b = 0.7$ kpc (Yang et al. 2012; Fujita et al. 2014). The influence of gravity was minor because supersonic flows were considered.

2.2 Energy injection

We considered two energy-injection types. One is the wind type, in which a constant wind blows from the GC for a period of $0 < t < t_0$, where $t = t_0$ is the current time. Specifically, the wind blows into the galactic halo, and two shock waves are formed. One is the forward shock, which propagates in the galactic halo gas, and the other is the reverse shock, which propagates in the wind gas (Fig. 1). In this context, the wind gas can be regarded as ejecta from the GC. A contact discontinuity or boundary between the halo gas and ejecta exists between the two shocks. As for the wind type, we considered two models. One is the wind-K model, in which we assumed that the wind is cold at the boundary. Another is the wind-T model, in which the wind gas has a large thermal energy

The other energy-injection type is the explosion type, for which energy is instantaneously injected into the GC at $t = 0$ as a single explosion. We also consider two models for this type. In the explosion-K model, the energy is given as the kinetic energy of the ejecta. Another one is the explosion-T model, in which the explosion energy is given as the thermal energy of the ejecta. As in the wind type, the forward shock is formed in the halo gas, the reverse shock is formed in the ejecta, and there is contact discontinuity between the two shocks.

At $t = 0$, the halo gas is in hydrostatic equilibrium and is

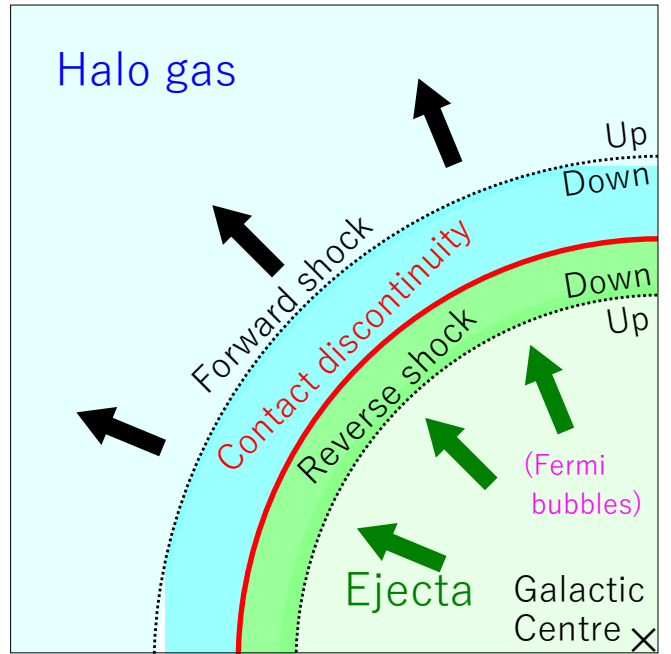


Figure 1. Schematic of the structures surrounding the Fermi bubbles. Cyan and green areas are filled with halo gas and ejecta (wind gas), respectively. The contact discontinuity (red solid line) is the boundary between the two gases. The forward and reverse shocks are shown by the black dotted lines; the upstream side and the downstream side of each shock are indicated by “Up” and “Down,” respectively. Regions heated by the forward and reverse shocks are shown in dark colours. The gamma-ray emitting Fermi bubbles correspond to the region inside the reverse shock (light green).

isothermal ($T = 0.2$ keV; Yoshino et al. 2009). We set the inner boundary at $r_{\text{in}} = 1$ (wind models) or 0.5 kpc (explosion models), and the outer boundary at $r_{\text{out}} = 15$ kpc from the GC. The results were insensitive to the boundary positions when the wind or explosion conditions were the same. The initial halo gas density at $r = r_{\text{in}}$ is treated as a parameter (ρ_1). In the wind models, we injected the wind (ejecta) gas at $r = r_{\text{in}}$ with velocity u_{w1} and density ρ_{w1} . In the wind-K model, the thermal energy of the wind at $r = r_{\text{in}}$ is assumed to be negligible. In the wind-T model, the wind gas has thermal energy of 3.1 keV per particle at $r = r_{\text{in}}$. The value of 3.1 keV does not have a solid physical meaning. We adopted it because it is much larger than the temperature of the gas around the Galactic centre (~ 0.7 keV; e.g. Nakashima et al. 2019) and that of the halo gas ($T = 0.2$ keV). Thus, the flow of 3.1 keV should be regarded as an extreme case of hot outflows, and the actual flow is likely to have a much lower thermal energy.

In the explosion-K model, the energy of the ejecta (E_{exp}) is given in the form of kinetic energy. The ejecta of a mass of M_{ej} with kinetic energy of E_{exp} is uniformly distributed at $r_{\text{in}} = 0.5 < r < 1$ kpc at $t = 0$. The velocity of the ejecta is given such that it increases linearly at $0.5 < r < 1$ kpc. The initial thermal energy of the ejecta was zero. In the explosion-T model, the ejecta of a mass of M_{ej} with thermal energy of E_{exp} is uniformly distributed at $0.5 < r < 1$ kpc at $t = 0$, and the ejecta is initially at rest.

3 RESULTS

We compared the simulation results with the observed profiles recently obtained by reanalysing the data from the Suzaku satellite, which has a high sensitivity to diffuse X-ray emissions (Yamamoto et al. 2022). In previous X-ray spectral analysis (e.g. Kataoka et al. 2013; LaRocca et al. 2020), the collisional equilibrium (CIE) state was assumed and a plasma model (`apec`) representing the CIE was used. However, the CIE is not guaranteed for the Fermi bubbles because the gas density is low and collisions between the gas particles are not frequent. In particular, the ionisation temperature at a shock may not be equal to either the kinetic temperature of the electrons or that of protons¹, because the heating of the plasma occurs in a very short timescale compared to the relaxation time. Therefore, in their reanalysis, Yamamoto et al. (2022) adopted a plasma model (`nei`) representing the non-equilibrium ionisation (NEI) state and found that `nei` actually reproduces the observed spectra better than `apec`. The X-ray spectrum of the NEI plasma is different from that of the CIE plasma, and the degree of the difference depends on the time lapsed since the plasma is forced out of equilibrium. The `nei` model can evaluate this time, and it can be interpreted as the shock age. This approach has often been adopted for supernova remnants (e.g. Safi-Harb et al. 2001) and clusters of galaxies (e.g. Fujita et al. 2008).

Yamamoto et al. (2022) derived the profiles of the density n_e , temperature kT , and shock age for a part of the X-ray bright regions surrounding the Fermi bubbles (North Polar Spur/Loop I). The observed temperature increases toward the inner ($r \sim 4$ kpc) and outer ($r \sim 6.5$ kpc) edges of the structure, while the density and shock age peak around the middle (Figs. 2 and 3). Here, we assumed that the distance to the GC is 8 kpc.

To best reproduce the observed profiles (density, temperature, and shock age), four simulation parameters were adjusted. For the wind models, the parameters were the current time t_0 , wind velocity (u_{w1}), wind density (ρ_{w1}), and initial density of the halo gas (ρ_1) at $r = 1$ kpc from the GC. The explosion model includes t_0 , total ejecta mass (M_{ej}), total explosion energy (E_{exp}), and ρ_1 . We performed $\sim 10^4$ simulations for each model to determine the parameters that reproduced the observed profiles. We choose only the simulation results in which the reverse shock is at $r = 4.0 \pm 0.2$ kpc, and the forward shock is at $r = 6.5 \pm 0.2$ kpc at $t = t_0$. We needed these constraints because the data of density, temperature, and shock age are not available on the upstream sides of both reverse and forward shocks ($r \lesssim 4.0$ kpc and $r \gtrsim 6.5$ kpc) due to low X-ray brightness. Without these data, the density and temperature jumps across the shocks cannot be identified in the fittings. On the other hand, the positions of the shocks are obvious from ROSAT X-ray images (Yamamoto et al. 2022).

We simultaneously fitted the simulated profiles to the observed profiles. The fits were performed in logarithmic parameter spaces. The best-fit parameters, the associated χ^2 values, and the degree of freedom (dof) are shown in Table 1. The

simulation results with the best fit parameters are presented in Figs 2 and 3. Although the density and shock age profiles are similar among the two wind and explosion-T models, the temperature and velocity profiles are intrinsically different. While the wind models reproduce all observed density, temperature, and shock age profiles, the explosion models does not reproduce the temperature profile. In the explosion-K model (Fig. 3a), the sharp density peak between the reverse shock and contact discontinuity is inconsistent with the observations. The peak height of the density is $\sim 0.06 \text{ cm}^{-3}$.

In the wind models (Fig. 2), the forward and reverse shocks initially formed at the contact discontinuity, where the shock age is the largest. Subsequently, the gas on the downstream sides of both shocks was considerably heated. Currently, the inner temperature peak ($r \sim 4$ kpc) corresponds to the reverse shock, and the outer peak ($r \sim 6.4$ kpc) corresponds to the forward shock. In the wind-K model, the reverse shock is powered by a fast wind blowing from the GC. The wind velocity is almost constant on the upstream side of the revised shock ($u_w \sim 1100 \text{ km s}^{-1}$ at $r < 4$ kpc; bottom of Fig. 2a). This large wind velocity results in a drastic velocity decrease to $u_w \sim 500 \text{ km s}^{-1}$ at the reverse shock, thereby converting the large kinetic energy into thermal energy and creating a sharp temperature peak. The contact discontinuity between the wind gas (ejecta) and halo gas is at the peak of the density and shock age profiles and at the trough of the temperature profile. We note that the sharp temperature peak at $r \sim 4.8$ kpc in Fig. 2a is a numerical artifact at the contact discontinuity. The wind-T model shows a similar behaviour (Fig. 2b). In this model, although the wind velocity at $r = r_{in}$ kpc (u_{w1}) is only 170 km s^{-1} (Table 1), it increased to $\sim 1000 \text{ km s}^{-1}$ slightly upstream of the reverse shock ($r \lesssim 4$ kpc; Fig. 2b), which is comparable to that in the wind-K model (Fig. 2a). By contrast, for the explosion models (Fig. 3), a prominent temperature peak is not observed at the reverse shock ($r \sim 3.8$ kpc), although a minor temperature increase exists there. According to this model, the ejecta expanded after the explosion. However, the expansion rate has decreased substantially over the last $t_0 \sim 6 \times 10^6$ yr (Table 1), and the velocity peak at the reverse shock is at most comparable to that at the forward shock. Thus, the velocity decrease at the reverse shock is moderate, which results in less thermal energy creation and no temperature peak. Therefore, the temperature profile is not consistent with observations.

The value of χ^2/dof of the wind-K model is close to one (Table 1), which means that this model successfully reproduced the observations. The value of χ^2/dof of the wind-T model is almost the same as that of the wind-K model, which means that the influence of thermal energy is minor. On the other hand, the values of χ^2/dof of the explosion models are much larger than one (Table 1), and they are inconsistent with the observations. The success of the wind model implies that the duration of the GC activities ($\sim 10^7$ yr) was not instantaneous. We assumed that the halo gas was in the CIE state before the wind began blowing. Since the NEI state returns to the CIE state in a time-scale of

$$t_{\text{CIE}} \sim 10^7 \left(\frac{n_e}{3 \times 10^{-3} \text{ cm}^{-3}} \right)^{-1} \text{ yr} \quad (5)$$

(Smith & Hughes 2010; Yamamoto et al. 2022), any wind episodes before that period do not affect our results. Our results ($t_0 \sim 10^7$ yr) may indicate that the duty cycle of

¹ On the downstream side of the shocks we considered, we assume that the electron temperature has well approached the proton temperature through Coulomb interaction and other mechanisms (e.g. waves excited by plasma instabilities; Bohdan et al. 2020).

Table 1. Best-fit parameters.

Models	t_0 (yr)	u_{w1} (km s $^{-1}$)	ρ_{w1}/m_p^1 (cm $^{-3}$)	M_{ej} (M_\odot)	E_{exp} (erg)	ρ_1/m_p^1 (cm $^{-3}$)	χ^2/dof
wind-K	9.0×10^6	1.1×10^3	9.3×10^{-3}	0.024	51.7/56
wind-T	9.1×10^6	1.7×10^2	5.3×10^{-2}	0.017	55.8/55
explosion-K	6.5×10^6	3.9×10^7	3.0×10^{56}	0.027	190.0/54
explosion-T	5.7×10^6	4.2×10^7	6.7×10^{56}	0.032	242.3/56

1m_p is the proton mass.

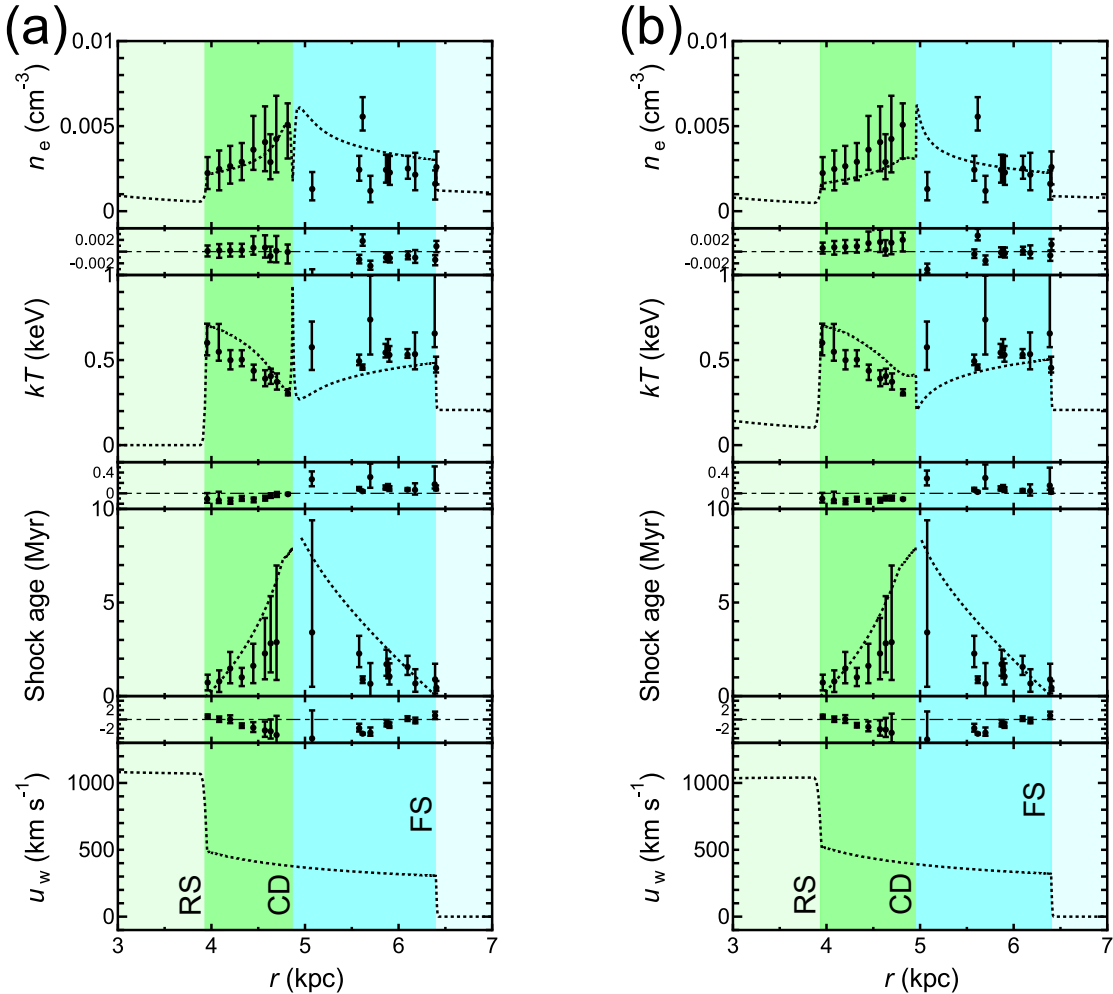


Figure 2. The gas profiles for (a) wind-K model, and (b) wind-T model. The panels are electron density (top), temperature (upper middle), shock age (lower middle), and velocity (bottom) at $t = t_0$ (current time). The simulation results are shown by the dotted lines, and the observations are shown by the dots (Yamamoto et al. 2022). For the latter, the errors are 1σ , and the angular size is transformed into the radius, assuming that the distance to the GC is 8 kpc. Residual plots are given underneath each of the panels. The colours correspond to those in Fig. 1. The boundaries are the reverse shock (RS), the contact discontinuity (CD), and the forward shock (FS).

Galactic centre activity is $\gtrsim 10^7$ yr. We cannot deny the possibility that a similar episode of energy injection rendered the halo gas non-equilibrium $\gg 10^7$ yr before.

We note that the actual wind may be multi-phase. In the above calculations, we implicitly assumed that one phase is dominant over other phases in the wind gas. However, while the wind-K and -T models have different initial temperatures, they give similar results (Fig. 2). This implies that even

if one phase is not dominant, the overall structure would not change much.

4 DISCUSSION

The wind power and mass flux obtained above offer clues regarding the origin of the Fermi bubbles. The best-fit wind-K model indicates that the energy injection rate is $L_w =$

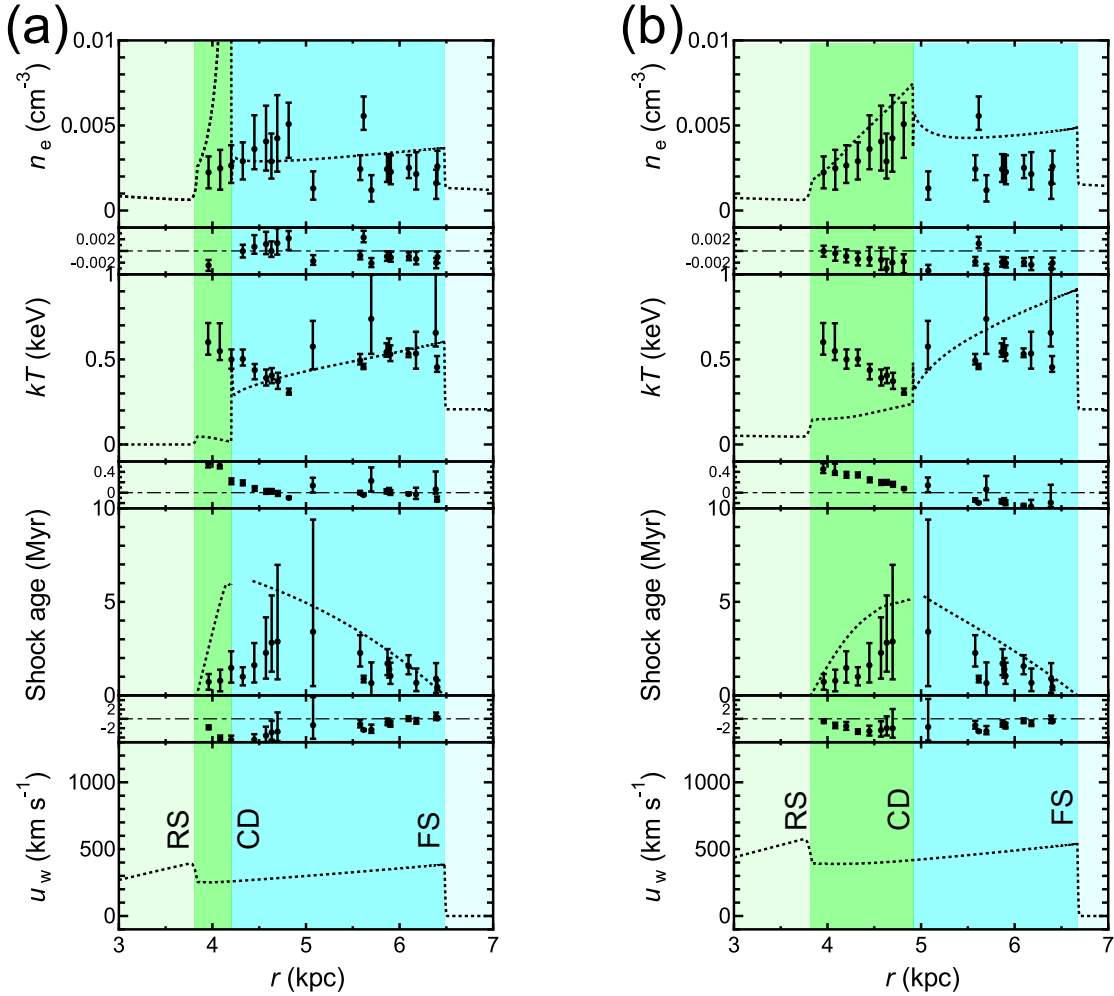


Figure 3. Same as Fig. 2 but for (a) explosion-K model, and (b) explosion-T model.

$1.4 \times 10^{42} \text{ erg s}^{-1}$. Given the mass of the supermassive black hole in the GC ($\sim 4 \times 10^6 M_{\odot}$; [Boehle et al. 2016](#); [Gillessen et al. 2017](#)), L_w is much smaller than the theoretical maximum rate given by the Eddington limit ($\sim 5 \times 10^{44} \text{ erg s}^{-1}$). Thus, the black hole can provide sufficient power to propagate the wind. This is in contrast to the explosion model, in which the energy input must be instantaneous and as powerful as the Eddington limit. The best-fit wind model also indicated that the mass flux is $\dot{M} = 3.4 M_{\odot} \text{ yr}^{-1}$. The large flux suggests that the wind is not directly produced near the black hole but is formed as light energetic outflows from the black hole entraining the surrounding interstellar gas. For example, because the black hole in the GC is surrounded by a massive molecular cloud ($\sim 3 \times 10^7 M_{\odot}$) called the central molecular zone ([Molinari et al. 2011](#)), a fraction of the cold gas may be blown out and become the wind. The cold (~ 10 – 100 K) gas outflow observed around the GC ([Di Teodoro et al. 2020](#)) may be remnants of the windblown cold gas. The existence of high-velocity, low-metallicity clouds may indicate that even clouds in the halo have been blown away ([Ashley et al. 2022](#), see also [Fox et al. 2015](#); [Bordoloi et al. 2017](#); [Karim et al. 2018](#); [Ashley et al. 2020](#)). In addition, warm ($\sim 10^3$ – 10^5 K) and hot ($\gtrsim 10^6$ K) interstellar gases around the GC may be accelerated. Notably, outflows of warm and hot gases have

been observed around the GC ([McClure-Griffiths et al. 2013](#); [Fox et al. 2015](#); [Nakashima et al. 2019](#); [Ponti et al. 2019](#)). These multiphase gases may have mixed, becoming the wind blowing into the Fermi bubbles. To entrain a large amount of gas ($\dot{M} = 3.4 M_{\odot} \text{ yr}^{-1}$), the initial gas flows generated near the black hole should have wide opening angles, say ~ 60 – 100° , and large cross-sectional areas. Therefore, they are unlikely to be thin jets. This type and scale of outflows are often observed around active galactic nuclei (AGN) in other galaxies ([Tombesi et al. 2013, 2014](#); [Laha et al. 2021](#); [Byun et al. 2022](#)). Thus, the formation of the wind and the process of mass loading around the GC may be similar to those of AGN outflows ([King & Pounds 2015](#); [Cecil et al. 2021](#) see also [Soker et al. 2009](#)). The current level of activity of Sagittarius A* is much lower than L_w , suggesting that the activity ceased only recently or fluctuated on a time scale much shorter than the wind period of $\sim 10^7$ yr ([Koyama et al. 1996](#); [Totani 2006](#); [Bland-Hawthorn et al. 2013, 2019](#)). If the activity ceases, the mass flux of the wind should decrease near the GC. On the other hand, the star formation activity and associated supernova explosions around the GC are unlikely to be the energy sources of the fast wind and Fermi bubbles. This is because the star formation rate around the GC has been only $\sim 0.1 M_{\odot} \text{ yr}^{-1}$ for the past $\gtrsim 10^6$ yr ([Yusef-Zadeh](#)

et al. 2009; Immer et al. 2012), which suggests that the power provided by the activity is only $\sim 10^{40}$ erg s $^{-1}$ (Crocker et al. 2015).

The AGN outflows in other galaxies are thought to regulate the growth of the galaxies and black holes (King & Pounds 2015); therefore, it may be natural that the same phenomenon occurs in the Milky Way Galaxy. If the wind blowing into the Fermi bubbles is the same as the AGN outflows, the proximity of the GC can allow us to closely study the nature of the AGN outflows. Moreover, the temperature and shock age of the gas associated with the Fermi bubbles will soon be measured more precisely with the X-Ray Imaging and Spectroscopy Mission (XRISM) satellite with an exceptional energy resolution (Tashiro et al. 2020, see also Inoue et al. 2015). The XRISM satellite can also directly measure X-ray gas velocity for the first time. The velocity gradient in the high-density region ($r \sim 4\text{--}6.5$ kpc) is particularly useful because the gradient differs between the wind and explosion models (Figs. 2 and 3). Observations of the gas velocity around the GC could also be helpful in understanding the mass loading process of the wind.

Although our results indicate the existence of a strong reverse shock, prominent non-thermal emissions have not been observed there. This may imply that the efficiency of particle acceleration is small. One possibility is that magnetic fields on the upstream side of the shock are turbulent. This may be expected if the winds from the GC are not laminar. If the magnetic fields are turbulent in the upstream region, the particles are trapped by the fields and just swept downstream with the fluids. The particles are not allowed to go back and forth across the shock. As a result, the mechanism of diffusive shock acceleration (DSA) does not work (Takamoto & Kirk 2015).

Finally, we should discuss caveats on the use of 1D simulations in this work. Since the actual Fermi bubbles are two bubbles elongated perpendicular to the Galactic plane, our 1D model cannot precisely reproduce the bubbles, especially for $\lesssim 2$ kpc above or below the Galactic disk, where they are heavily distorted by the dense disk as is suggested by the gamma-ray images (Su et al. 2010; Ackermann et al. 2014). However, since radiative cooling is inefficient, the evolution of the bubbles is rather simple. Moreover, the impact of the non-spherical gravity on the bubble evolution is minor as long as the expansion is supersonic. Thus, our model should reproduce the actual bubbles at least qualitatively. Even quantitatively, our results are not much different from those of multi-dimensional simulations, given a bubble volume. For example, the wind-K model requires total energy of $\sim 4 \times 10^{56}$ ergs, which is consistent with those derived through 3D wind simulations by Mou et al. (2014) within an order of magnitude. Our value is larger than those obtained by Mou et al. (2014) probably because the 1D bubble expands at a low altitude (closer to the Galactic plane) where the density of the halo gas is larger. The existence of the wind of ~ 1000 km s $^{-1}$ is robust, because the height of the temperature peak at the reverse shock simply reflects the upstream velocity.

5 CONCLUSION

We have studied the properties of the non-equilibrium X-ray gas structures around the Fermi bubbles. Using numer-

ical simulations, we showed that a combination of the density, temperature, and shock age profiles can be a useful tool to identify the energy injection mechanism at the GC. By comparing the results of numerical simulations with observations, we found that the Fermi bubbles were most likely to be created by a fast wind from the GC, which had a speed of ~ 1000 km s $^{-1}$, and blew for $\sim 10^7$ yr. The wind generates a strong reverse shock and reproduces a sharp temperature increase as is observed. On the other hand, models in which energy was instantaneously injected cannot reproduce the observed temperature profile. Considering the power of the wind, the energy source seems to be Sagittarius A*, and not star formation activities. Since the mass flux of the wind is large, interstellar gas might have been entrained by the wind. For the entrainment, the initial outflows launched in the vicinity of the black hole should have a large opening angle and they are not likely to be thin jets. The outflows may be the same as AGN outflows that are often observed in other galaxies.

ACKNOWLEDGEMENTS

We would like to thank the anonymous referee for a constructive report. Y.F. was supported by JSPS KAKENHI 20H00181, 22H00158, 22H01268.

DATA AVAILABILITY

The data generated from computations are reported in the paper and any additional data will be made available upon reasonable request to the corresponding author.

REFERENCES

- Ackermann M., et al., 2014, *ApJ*, **793**, 64
 Ashley T., Fox A. J., Jenkins E. B., Wakker B. P., Bordoloi R., Lockman F. J., Savage B. D., Karim T., 2020, *ApJ*, **898**, 128
 Ashley T., Fox A. J., Cashman F. H., Lockman F. J., Bordoloi R., Jenkins E. B., Wakker B. P., Karim T., 2022, arXiv e-prints, p. arXiv:2207.08838
 Bland-Hawthorn J., Cohen M., 2003, *ApJ*, **582**, 246
 Bland-Hawthorn J., Maloney P. R., Sutherland R. S., Madsen G. J., 2013, *ApJ*, **778**, 58
 Bland-Hawthorn J., et al., 2019, *ApJ*, **886**, 45
 Bodenheimer P., Laughlin G. P., Rozyczka M., Yorke H. W., 2007, Numerical Methods in Astrophysics: An Introduction, CRC Press, Boca Raton
 Boehle A., et al., 2016, *ApJ*, **830**, 17
 Bohdan A., Pohl M., Niemiec J., Morris P. J., Matsumoto Y., Amano T., Hoshino M., 2020, *ApJ*, **904**, 12
 Bordoloi R., et al., 2017, *ApJ*, **834**, 191
 Byun D., Arav N., Hall P. B., 2022, *ApJ*, **927**, 176
 Carretti E., et al., 2013, *Nature*, **493**, 66
 Cecil G., Wagner A. Y., Bland-Hawthorn J., Bicknell G. V., Mukherjee D., 2021, *ApJ*, **922**, 254
 Crocker R. M., 2012, *MNRAS*, **423**, 3512
 Crocker R. M., Aharonian F., 2011, *Phys. Rev. Lett.*, **106**, 101102
 Crocker R. M., Bicknell G. V., Taylor A. M., Carretti E., 2015, *ApJ*, **808**, 107
 Di Teodoro E. M., McClure-Griffiths N. M., Lockman F. J., Armillotta L., 2020, *Nature*, **584**, 364
 Dobler G., Finkbeiner D. P., 2008, *ApJ*, **680**, 1222

- Dobler G., Finkbeiner D. P., Cholis I., Slatyer T., Weiner N., 2010, *ApJ*, **717**, 825
- Finkbeiner D. P., 2004, *ApJ*, **614**, 186
- Fox A. J., et al., 2015, *ApJ*, **799**, L7
- Fujita Y., et al., 2008, *PASJ*, **60**, 1133
- Fujita Y., Ohira Y., Yamazaki R., 2013, *ApJ*, **775**, L20
- Fujita Y., Ohira Y., Yamazaki R., 2014, *ApJ*, **789**, 67
- Gillessen S., et al., 2017, *ApJ*, **837**, 30
- Guo F., Mathews W. G., 2012, *ApJ*, **756**, 181
- Immer K., Schuller F., Omont A., Menten K. M., 2012, *A&A*, **537**, A121
- Inoue Y., Nakashima S., Tahara M., Kataoka J., Totani T., Fujita Y., Sofue Y., 2015, *PASJ*, **67**, 56
- Karim T., et al., 2018, *ApJ*, **860**, 98
- Kataoka J., et al., 2013, *ApJ*, **779**, 57
- Keshet U., Gurwich I., 2018, *MNRAS*, **480**, 223
- King A., Pounds K., 2015, *ARA&A*, **53**, 115
- Koyama K., Maeda Y., Sonobe T., Takeshima T., Tanaka Y., Yamauchi S., 1996, *PASJ*, **48**, 249
- LaRocca D. M., Kaaret P., Kuntz K. D., Hodges-Kluck E., Zajczyk A., Bluem J., Ringuette R., Jahoda K. M., 2020, *ApJ*, **904**, 54
- Lacki B. C., 2014, *MNRAS*, **444**, L39
- Laha S., Reynolds C. S., Reeves J., Kriss G., Guainazzi M., Smith R., Veilleux S., Proga D., 2021, *Nature Astronomy*, **5**, 13
- McClure-Griffiths N. M., Green J. A., Hill A. S., Lockman F. J., Dickey J. M., Gaensler B. M., Green A. J., 2013, *ApJ*, **770**, L4
- Miyamoto M., Nagai R., 1975, *PASJ*, **27**, 533
- Molinari S., et al., 2011, *ApJ*, **735**, L33
- Mondal S., Keshet U., Sarkar K. C., Gurwich I., 2022, *MNRAS*, **514**, 2581
- Mou G., Yuan F., Bu D., Sun M., Su M., 2014, *ApJ*, **790**, 109
- Mou G., Yuan F., Gan Z., Sun M., 2015, *ApJ*, **811**, 37
- Nakashima S., Koyama K., Wang Q. D., Enokiya R., 2019, *ApJ*, **875**, 32
- Narayanan S. A., Slatyer T. R., 2017, *MNRAS*, **468**, 3051
- Planck Collaboration 2013, *A&A*, **554**, A139
- Ponti G., et al., 2019, *Nature*, **567**, 347
- Predehl P., et al., 2020, *Nature*, **588**, 227
- Safi-Harb S., Harrus I. M., Petre R., Pavlov G. G., Koptsevich A. B., Sanwal D., 2001, *ApJ*, **561**, 308
- Salter C. J., 1983, *Bulletin of the Astronomical Society of India*, **11**, 1
- Sarkar K. C., Nath B. B., Sharma P., 2015, *MNRAS*, **453**, 3827
- Smith R. K., Hughes J. P., 2010, *ApJ*, **718**, 583
- Snowden S. L., et al., 1995, *ApJ*, **454**, 643
- Sofue Y., 2000, *ApJ*, **540**, 224
- Soker N., Sternberg A., Pizzolato F., 2009, in Heinz S., Wilcots E., eds, *American Institute of Physics Conference Series* Vol. 1201, *The Monster's Fiery Breath: Feedback in Galaxies, Groups, and Clusters*. pp 321–325 ([arXiv:0909.0220](https://arxiv.org/abs/0909.0220)), [doi:10.1063/1.3293066](https://doi.org/10.1063/1.3293066)
- Su M., Slatyer T. R., Finkbeiner D. P., 2010, *ApJ*, **724**, 1044
- Takamoto M., Kirk J. G., 2015, *ApJ*, **809**, 29
- Tashiro M., et al., 2020, in *Society of Photo-Optical Instrumentation Engineers (SPIE) Conference Series*. p. 1144422, [doi:10.1117/12.2565812](https://doi.org/10.1117/12.2565812)
- Tombesi F., Cappi M., Reeves J. N., Nemmen R. S., Braitto V., Gaspari M., Reynolds C. S., 2013, *MNRAS*, **430**, 1102
- Tombesi F., Tazaki F., Mushotzky R. F., Ueda Y., Cappi M., Gofford J., Reeves J. N., Guainazzi M., 2014, *MNRAS*, **443**, 2154
- Totani T., 2006, *PASJ*, **58**, 965
- Yamamoto M., Kataoka J., Sofue Y., 2022, *MNRAS*, **512**, 2034
- Yang H. Y. K., Ruszkowski M., Ricker P. M., Zweibel E., Lee D., 2012, *ApJ*, **761**, 185
- Yang H. Y. K., Ruszkowski M., Zweibel E. G., 2022, *Nature Astronomy*, **6**, 584
- Yoshino T., et al., 2009, *PASJ*, **61**, 805
- Yusef-Zadeh F., et al., 2009, *ApJ*, **702**, 178
- Zhang R., Guo F., 2020, *ApJ*, **894**, 117
- Zubovas K., Nayakshin S., 2012, *MNRAS*, **424**, 666

This paper has been typeset from a $\text{\TeX}/\text{\LaTeX}$ file prepared by the author.